J. Fluid Mech. (2011), *vol.* 678, *pp.* 271–293.
doi:10.1017/jfm.2011.115

Decay of an internal tide due to random topography in the ocean

OLIVER BÜHLER† AND MIRANDA HOLMES-CERFON‡
Courant Institute of Mathematical Sciences, New York University, New York, NY 10012, USA

(Received 17 September 2010; revised 16 February 2011; accepted 2 March 2011;
first published online 18 April 2011)

We present a theoretical and numerical study of the decay of an internal wave caused by scattering at undulating sea-floor topography, with an eye towards building a simple model in which the decay of internal tides in the ocean can be estimated. As is well known, the interactions of internal waves with irregular boundary shapes lead to a mathematically ill-posed problem, so care needs to be taken to extract meaningful information from this problem. Here, we restrict the problem to two spatial dimensions and build a numerical tool that combines a real-space computation based on the characteristics of the underlying partial differential equation with a spectral computation that satisfies the relevant radiation conditions. Our tool works for finite-amplitude topography but is restricted to subcritical topography slopes. Detailed results are presented for the decay of the gravest vertical internal wave mode as it encounters finite stretches of either sinusoidal topography or random topography defined as a Gaussian random process with a simple power spectrum. A number of scaling laws are identified and a simple expression for the decay rate in terms of the power spectrum is given. Finally, the resulting formulae are applied to an idealized model of sea-floor topography in the ocean, which seems to indicate that this scattering process can provide a rapid decay mechanism for internal tides. However, the present results are restricted to linear fluid dynamics in two spatial dimensions and to uniform stratification, which restricts their direct application to the real ocean.

Key words: internal waves, topographic effects, wave scattering

1. Introduction

1.1. *Internal tides in the ocean*

Internal gravity waves are an essential component of the dynamics of the ocean. Not only are they the most energetic form of fluid motion at small scales, but they also provide an important contribution to small-scale mixing, especially in the vertical, via the three-dimensional (3D) turbulence that is induced in localized regions where the waves are unstable and break. Broadly speaking, such turbulent vertical mixing across the stable stratification surfaces of constant density, say, is vital for the functioning of a global ocean overturning circulation, in which particles must

† Email address for correspondence: obuhler@cims.nyu.edu
‡ Current address: School of Engineering and Applied Sciences, Harvard University, Cambridge, MA 02138, USA.

be allowed to cross these density surfaces. It is believed that the breaking of small-scale internal waves in the ocean interior, together with cross-stratification mixing at outcropping stratification surfaces at the ocean surface and the sea floor, is the major agent for 'lubricating' the vertical branches of the global overturning circulation (e.g. Kunze & Llewellyn Smith 2004; Wunsch & Ferrari 2004). The details of the interplay between wave-induced small-scale mixing and the large-scale ocean circulation are still actively debated today, but certainly all current numerical ocean models include a parameterization of such wave-induced interior vertical mixing in order to be able to simulate a realistic ocean circulation.

In this area much recent research has been devoted to the role of internal tides, i.e. internal waves connected to the lunar or solar gravitational tidal forcing. Here the emphasis has been on the semi-diurnal, M_2 tide and especially on the process of so-called tidal conversion, in which the barotropic, depth-independent M_2 tide generates new internal tides with non-zero vertical wavenumbers via interaction with undulating sea-floor topography (e.g. Balmforth, Ierley & Young 2002; Garrett 2003; Llewellyn Smith & Young 2003; Petrelis, Smith & Young 2006; Bühler & Muller 2007; Garrett & Kunze 2007; Balmforth & Peacock 2009; Muller & Bühler 2009). The concomitant conversion of barotropic tidal energy into wave energy at smaller scales is viewed as a first step in a cascade of energy to smaller scales that ultimately provides the turbulent energy required for the vertical mixing.

Theoretical and observational studies of tidal conversion at isolated large topography features such as the Hawaiian ridge have suggested that a large fraction of the internal tide energy so generated propagates away from the feature in the form of modes with very low vertical wavenumber (e.g. St Laurent & Garrett 2002). This raises the question of how far these low-wavenumber modes can propagate in the horizontal before they have lost their energy to other forms of motion (e.g. Alford 2003; Zhao *et al.* 2010). This is an important question not least because it is a central tenet of wave–mean interaction theory that the mean circulation typically 'feels' the presence of waves not at their generation site, but at their dissipation site (e.g. Bühler 2009). So it makes a difference whether such low-wavenumber tides can propagate a few hundred or tens of thousands of kilometres away from their site of generation.

There are a number of dynamical mechanisms that can draw energy from an internal wave, for example nonlinear wave–wave interactions with other internal waves, or nonlinear interactions between the waves and the slower mean circulation. However, in this paper we are looking at a linear mechanism, namely the interactions of a propagating wave mode with rough sea-floor topography that we model as a random function. The rough topography scatters the incoming wave into other spectral components and by this simple process draws energy away from the primary wave. Our aim is to show that this provides a surprisingly efficient decay mechanism even for random, irregular topography.

1.2. *Modelling wave interactions with sea-floor topography*

This would appear to be a standard wave problem that should hold no surprises, but the mathematical problem for studying this scattering process involving internal waves is actually very unusual, because it involves solving a hyperbolic partial differential equation (PDE) for the spatial structure of the waves. Indeed, in two spatial dimensions, which is the idealized case we look at here, the governing PDE can be solved formally using the method of characteristics. This leads to the well-known fact that the problem of computing the spatial structure of internal wave in bounded domains is an ill-posed mathematical problem, a fact that has been discovered and

rediscovered numerous times in the fluid literature; for example, Sobolev noted it in the context of the mathematically analogous problem of wave motion in rotating containers such as fuel tanks for rockets (see p. 335ff. in Arnold & Khesin 1998, who gave the reference Sobolev 1954). The physical manifestation of the ill-posedness is the focusing of wave energy in small regions, which then become the natural seeds for wave instability and breaking. Under suitable conditions the location of the wave focusing regions can be analysed using dynamical systems methods and by now this is a well-understood problem (e.g. Maas & Lam 1995).

Earlier work directly related to this problem in oceanography includes the study of wave-beam reflection by Longuet-Higgins (1969) and the papers by Muller & Xu (1992) and Muller & Liu (2000*a*,*b*) on oceanic internal wave scattering. In the present paper, we combine and slightly extend techniques from these papers to build a numerical tool with which we can study the decay of a mode-one internal tide due to interactions with sea-floor topography over a substantial length of propagation. As is clearly laid out in Muller & Liu (2000*a*), this requires combining the method of characteristics with a spectral method in order to satisfy the horizontal radiation conditions for the scattering problem.

To make progress, we make a number of simplifying assumptions, namely we restrict to two dimensions (one horizontal and the other vertical), we ignore other fluid motion apart from the linear waves, and we treat the Coriolis frequency f and the buoyancy frequency N as constants. Treating f as a constant is quite realistic for the small-scale problem we are looking at, but N is a strong function of depth z in the real ocean, with very low values in the thin mixed layer on top of the ocean, higher values of N in the upper ocean, and then again much reduced values in the deep, abyssal ocean. In principle, this could lead to important wave reflection effects in regions of strong gradients of N. However, previous experience with variable N in studies of tidal conversion has indicated that very often allowing for variable N gently modifies but does not change in a fundamental way the results for constant N. Moreover, a recent study by Grimshaw, Pelinovsky & Talipova (2010) shows that there are realistic-looking profiles of $N(z)$ that are entirely reflection-free, i.e. for these profiles reflectionless Wentzel–Kramers–Brillouin (WKB)-theory for internal waves gives exactly the right answer. Still, it would of course be very useful to extend our results towards realistic profile for N. This is particularly important for comparison with observational ocean case studies.

Another simplifying assumption is that we assume that the topography is subcritical throughout, i.e. the topography slope is everywhere less than the natural propagation angle of the internal waves at the sea floor. This is a reasonable though not perfect assumption for ocean topography away from major ridges and isolated features. Notably, for our numerical tool we do *not* assume that the topography is small, just that its slope is less than a certain $O(1)$ value.

We applied our numerical tool to two kinds of topography: a stretch of deterministic sinusoidal topography and a stretch of random topography with specified covariance structure. In the first case, we obtain strong wave focusing if the wavenumber of the topography matches the wavenumber of a freely propagating internal mode in a finite-depth ocean. This is as expected from the previous work on wave focusing in bounded containers, to which the present situation is analogous in this case. This part of the paper is also well suited for comparisons with laboratory experiments.

In the case of random topography, which is the suitable case for the ocean application, we obtain scaling results for the exponential decay of the expected wave energy flux, at least in a certain limit of uncorrelated small-amplitude topography.

This leads to a very surprising expression for the exponential decay rate, because the decay rate appears to be independent of the values of N and f and even of the frequency of the primary tide. This surprising result could not have been derived using dimensional analysis.

We then apply our scheme to a simplified model spectrum for sea-floor topography in the ocean, for which we obtain a quantitative estimate for the exponential decay length that indicates that the scattering off the sea floor is a very efficient decay mechanism for the mode-one tide.

The outline of the paper is as follows. In § 2, the governing equations are formulated and the solution method is outlined in detail. In §§ 3 and 4, the wave focusing is examined for deterministic and random topography and is followed in § 5 by a detailed examination of the scaling laws for the decay rate in the random case. The application to the ocean spectrum is given in § 6 and concluding comments are offered in § 7.

2. Governing equations and solution method

2.1. *Governing equations*

We model the problem with the two-dimensional (2D) rotating linear Boussinesq system in a vertical slice geometry, in which all fields depend on the horizontal and vertical coordinates x and z only. Although the fields are independent of the other horizontal coordinate y, there is a non-zero velocity in the y-direction due to the Coriolis force. The governing equations for the velocity $\boldsymbol{u} = (u, v, w)$, buoyancy b and scaled perturbation pressure P are

$$u_t - fv + P_x = 0, \quad v_t + fu = 0, \quad w_t + P_z = b, \quad b_t + N^2 w = 0, \tag{2.1}$$

and the incompressibility constraint $u_x + w_z = 0$. Here the Coriolis parameter f and the buoyancy frequency N are both taken to be constant and we neglect 'non-traditional' vertical Coriolis forces.

Using a streamfunction $\psi(x, z, t)$ such that $u = \partial_z \psi$, $w = -\partial_x \psi$ reduces (2.1) to

$$(N^2 + \partial_{tt})\partial_{xx}\psi + (\partial_{tt} + f^2)\partial_{zz}\psi = 0. \tag{2.2}$$

This omits a steady balanced vortical solution described by the linear potential vorticity $q = v_x + fb_z/N^2$, which satisfies $q_t = 0$. However, for internal waves $q = 0$ everywhere and then (2.2) captures all the dynamics. We use a channel geometry with unbounded extent in the x-direction and rigid top and bottom boundaries at the ocean surface $z = H$ and the ocean floor $z = h(x)$. The no-normal-flow boundary conditions are

$$\psi(x, H, t) = \psi(x, h(x), t) = 0, \tag{2.3}$$

which excludes any net current along the channel. The sea-floor topography $h(x)$ is taken to be zero outside of a compact region $x \in [0, L]$, see figure 1. We do not require $h(x)/H$ to be infinitesimal, although we do assume that the slope $\mathrm{d}h(x)/\mathrm{d}x$ is subcritical in the sense defined below (2.6). We loosely call the *domain* of the problem a region whose horizontal extent is slightly larger than the region where $h(x)$ may vary, and speak of waves 'entering' or 'exiting' this domain in the sense of group velocity. The waves which enter the domain on the left are specified in advance while the transmitted waves on the right-hand boundary and the reflected waves on the left-hand boundary must then obey a horizontal radiation condition, which requires that any additional energy flux be directed away from the topography.

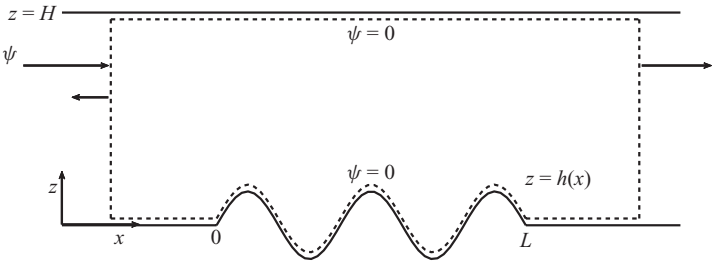

FIGURE 1. Geometry of the problem and boundary conditions. The domain is enclosed by a dashed line. The primary wave is incident from the left and scattering at the topography creates transmitted and reflected waves to the right and the left, respectively.

We look for time-periodic solutions with a given frequency such as the frequency of the M_2 internal tide, which we assume is above f and below N. Therefore, we fix $\omega > 0$ such that $N > \omega > f$ and look for solutions of the form

$$\psi(x, z, t) = \mathrm{Re}\Psi(x, z)\,\mathrm{e}^{-\mathrm{i}\omega t} \tag{2.4}$$

with the complex-valued function $\Psi(x, z)$ to be found. Notably, although the wave field is periodic in time, the horizontal radiation conditions provide a causal structure to the problem, so that we can think of waves entering from the left and decaying as they propagate to the right and so on, as in the usual construction of a causal solution to a dispersive wave problem.

All such internal waves travel at the same fixed angle with the vertical, which we scale to be 45°, and additionally we scale the ocean to have a depth of π over flat, zero topography. If we write non-dimensional variables with a prime then

$$(z, h) = \frac{H}{\pi}(z', h'), \quad x = \frac{1}{\mu}\frac{H}{\pi}x', \quad \text{where } \mu(\omega) = \sqrt{\frac{\omega^2 - f^2}{N^2 - \omega^2}} \tag{2.5}$$

is the slope of the waves. We assume that the topography is *subcritical* relative to the wave slope $\mu(\omega)$ in (2.5), i.e. the non-dimensional topography slope obeys $|\mathrm{d}h(x)/\mathrm{d}x| < 1$ for all x.

The non-dimensional equation for Ψ becomes, dropping the primes,

$$\Psi_{xx} - \Psi_{zz} = 0 \quad \text{and} \quad \Psi(x, \pi) = \Psi(x, h(x)) = 0. \tag{2.6}$$

Equation (2.6) is the one-dimensional (1D) wave equation, but with the twist that there is no time-like variable. In other words, the spatial structure of time-periodic internal waves is governed by a hyperbolic equation, as was noted a long time ago (Sobolev 1954).

Before moving on, we briefly discuss the typical values of μ for the M_2 tide in the ocean. Using a latitude of 30° the corresponding values for μ range from 0.04 to 0.2, with the low values found in the upper ocean where N is large (at about 1000 m depth, say), and the high values found near the sea floor where N is small. The higher local value of μ at the sea floor would be the relevant value to judge whether the topography is supercritical, whilst the smaller local value in the upper ocean is relevant to estimate the horizontal wavelength. The fact that these two different local values must be fused into one is an obvious shortcoming of the present model, which is restricted to constant stratification N. Incidentally, for the realistic-looking profiles of $N(z)$ considered in Grimshaw *et al.* (2010), it turns out that after a WKB-style rescaling of z and ψ the governing equation again has constant coefficients, but with

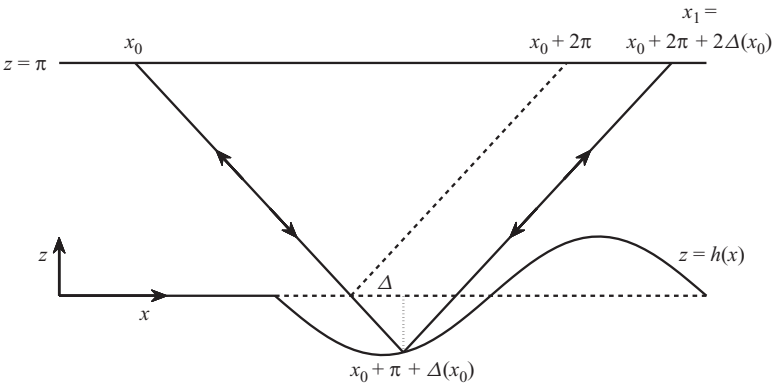

FIGURE 2. Characteristics and the horizontal shift Δ induced by undulating topography. As indicated, information travels in both directions along the characteristics. The shift function $\Delta(x)$ quantifies the horizontal shift of the reflection point compared to where it would have been if the topography were flat. Negative topography implies a positive shift and vice versa. By assumption all reflections are subcritical. Note that information flows in *both* directions along the characteristics.

an additional term in (2.6*a*) that is proportional to the streamfunction. Presumably, as the wave field develops smaller scales, the new term would become negligible compared to the derivatives term.

2.2. *Using characteristics, but not ray tracing*

Different analytical and numerical solution methods can be applied to (2.6). For example, for infinitesimal topography one can work with a wave-field expansion in terms of the propagating modes for zero topography. For finite-amplitude topography, an attractive numerical alternative is using a Green's function approach in which suitable sources are distributed along the topography (e.g. Petrelis *et al.* 2006; Echeverri & Peacock 2010). Here we choose to follow Muller & Liu (2000*a*) and use a combination of the method of characteristics plus a spectral scheme to satisfy the horizontal radiation condition for the scattered waves. Mathematically, this should lead to equivalent results as the Green's function method, but it is psychologically very different. At this stage, it is worth pointing out explicitly that using the method of characteristics for (2.6) is *not* the same as using group-velocity concepts and ray tracing. Indeed, here we do not make the assumption that the wave field can be described by a slowly varying wavetrain. This is a potentially confusing situation (e.g. Longuet-Higgins 1969) because the characteristic lines are identical to group-velocity rays in this problem, i.e. the characteristic slope $\mu(\omega)$ coincides with the group-velocity angle of plane internal waves with that frequency. The important difference is that there is a crucial two-way flow of information and energy along the characteristics but not along the one-way group-velocity rays (see figure 2). It is because of this two-way flow of information that the horizontal radiation conditions at both ends of the domain are important.

Now, the characteristics of (2.6) are the lines along which $x \pm z$ is constant and the general solution can then be written as

$$\Psi(x, z) = f(x + z - \pi) - f(x - z + \pi), \tag{2.7}$$

where use has been made of the homogeneous boundary condition at $z = \pi$. Clearly, the solution is determined everywhere once we know the complex-valued function $f(x)$ for all $x \in R$. Physically, $2f'(x) = \Psi_z = u$ at the ocean surface $z = \pi$.

It is useful to think of $f(x)$ as being defined along the ocean surface and then (2.7) expresses that the value of $\Psi(x, z)$ at any interior location can be found by tracing the leftward and rightward characteristics back up to the ocean surface and then subtracting the values of f that are found there. This puts non-trivial conditions on the functions $f(x)$ that correspond to solutions of this equation (e.g. Harlander & Maas 2007). Specifically, at the seafloor $z = h(x)$ we have $\Psi = 0$ and therefore the condition

$$f(x + h(x) - \pi) = f(x - h(x) + \pi) \tag{2.8}$$

must hold for all $x \in R$. Thus, if one follows a characteristic from left to right as it bounces up and down the ocean, then (2.8) implies that the same value of f recurs at every intersection of the chosen characteristic with the ocean surface. Clearly, over zero topography this means that $f(x)$ is periodic with period 2π and can hence be represented by a Fourier series with terms such as $f(x) \propto \exp(\mathrm{i}nx)$, where n is an integer. It then follows from (2.7) that to the right and to the left of the topography region the solution can be written in terms of discrete propagating modes of the form $\Psi = \sin(nz)\exp(\mathrm{i}nx)$. Here $n > 0$ corresponds to a rightward-propagating mode and vice versa, so the radiation condition for the scattered waves is that only $n > 0$ modes are allowed for $x > L$ and only $n < 0$ modes are allowed for $x < 0$.

We now establish the connection between $f(x)$ on the left and the right of the topography and then solve the full problem using the radiation condition.

2.3. *The characteristic map*

A rightward-moving characteristic emanating from a surface point reflects off the bottom with a slope of $+1$ and continues rightward, hitting the surface again some distance away from its starting location. This defines the *characteristic map* $R_n(x)$ such that if x is the initial horizontal position of a characteristic on the surface, then $R_n(x)$ is the horizontal position where it hits the surface again after n bounces. The interval between successive hitting points defines a *characteristic period*, whose length we abbreviate as the *period*. A single characteristic decomposes the domain into a disjoint sequence of characteristic periods. The map of a characteristic starting anywhere in the domain can be determined once we know the map of a single characteristic period, since each R_n is an order-preserving bijection from one characteristic period onto another.

The characteristic map after one rightward bounce is given by

$$R_1(x) = x + 2\pi + 2\Delta(x), \tag{2.9}$$

where the horizontal shift function $\Delta(x)$ captures the change in the map due to non-zero topography (see figure 2). By inspection, we see that for subcritical $h(x)$ the shift function $\Delta(x)$ is the unique solution to the nonlinear equation

$$h(x + \pi + \Delta(x)) + \Delta(x) = 0. \tag{2.10}$$

The map after n rightward bounces can be obtained inductively and is

$$R_{n+1}(x) = R_n(x) + 2\Delta(R_n(x)) + 2\pi. \tag{2.11}$$

As noted earlier, the top and bottom boundary conditions imply that $f(x) = f(R_1(x))$, so by induction for any n,

$$f(R_n(x)) = f(x), \quad f\left(R_n^{-1}(x)\right) = f(x). \tag{2.12}$$

Here $R_n^{-1}(x)$ denotes the inverse map, which corresponds to n leftward bounces.

For future reference, if we consider two neighbouring characteristics at x_n and $x_n + \delta_n$ and compute from (2.9–2.10) how their infinitesimal separation δ_n evolves we find that

$$\delta_{n+1} = \delta_n \, R_1'(x_n) = \delta_n \frac{1-s}{1+s}, \tag{2.13}$$

where s is the value of h' at the intersect with the topography. For example, if $s > 0$ then neighbouring characteristics contract. This relation is useful for understanding how the gradients of Ψ evolve and also for the consideration of random topography in § 4.2.

2.4. *Solution for the Fourier coefficients in terms of the characteristic map*

Let D_0 and D_1 be characteristic periods of period 2π to the far left and far right of the topography, respectively, such that $R_n(D_0) = D_1$ for some n. The function f can be written as a Fourier series on each interval. Because of the horizontal radiation condition it has the form

$$f(x) = f_0(x) + f_r(x), \; x \in D_0, \quad f(x) = f_t(x), \; x \in D_1, \tag{2.14}$$

where $f_0(x) = \sum_{k=1}^{\infty} a_k^0 \, \mathrm{e}^{\mathrm{i}kx}$, $x \in D_0$ are the prescribed incoming waves, $f_t(x) = \sum_{k=0}^{\infty} a_k^t \, \mathrm{e}^{\mathrm{i}kx}$, $x \in D_1$ are the transmitted waves, and $f_r(x) = \sum_{k=0}^{\infty} a_k^r \, \mathrm{e}^{-\mathrm{i}kx}$, $x \in D_0$ are the reflected waves.

Without loss of generality, we can set $a_0^t = 0$, since this constant can be absorbed into a_0^r. Substituting (2.14) into (2.12) and projecting onto the mth Fourier mode yields a system of equations for the coefficients of the waves (Muller & Liu 2000*a*):

$$\left.\begin{aligned} \boldsymbol{a}^t - D\boldsymbol{a}^r &= S\boldsymbol{a}^0, \\ \boldsymbol{a}^r &= B\boldsymbol{a}^t, \end{aligned} \qquad \begin{aligned} \boldsymbol{a}^0 &= \left(a_k^0\right)_{k=1}^{\infty}, \\ \boldsymbol{a}^t &= \left(a_k^t\right)_{k=1}^{\infty}, \\ \boldsymbol{a}^r &= \left(a_k^r\right)_{k=0}^{\infty}, \end{aligned} \right\} \tag{2.15}$$

where

$$\left.\begin{aligned} D &= (D_{mk})_{m=1,\ldots,\infty;k=0,\ldots,\infty}, \quad & D_{mk} &= \frac{1}{2\pi}\int_{D_1} \mathrm{e}^{-\mathrm{i}kR_n^{-1}(x)} \, \mathrm{e}^{-\mathrm{i}mx} \, \mathrm{d}x, \\ B &= (B_{mk})_{m=0,\ldots,\infty;k=1,\ldots,\infty}, \quad & B_{mk} &= \frac{1}{2\pi}\int_{D_0} \mathrm{e}^{\mathrm{i}kR_n(x)} \, \mathrm{e}^{\mathrm{i}mx} \, \mathrm{d}x, \\ S &= (S_{mk})_{m=1,\ldots,\infty;k=1,\ldots,\infty}, \quad & S_{mk} &= \frac{1}{2\pi}\int_{D_1} \mathrm{e}^{\mathrm{i}kR_n^{-1}(x)} \, \mathrm{e}^{-\mathrm{i}mx} \, \mathrm{d}x. \end{aligned} \right\} \tag{2.16}$$

By truncating the system after a certain number of modes, a solution is found numerically once the characteristic map $R_n(x)$ is known.

The PDE (2.6) conserves the vertically integrated energy flux, and in our scaled system $k|a_k|^2$ is the magnitude of the energy flux of a single plane wave over flat topography. Energy conservation together with orthogonality implies

$$\sum_{k=1}^{\infty} k|a_k^0|^2 = \sum_{k=1}^{\infty} k|a_k^t|^2 + \sum_{k=1}^{\infty} k|a_k^r|^2, \tag{2.17}$$

which says that the energy that enters the domain on the left is partially transmitted and partially reflected back. We used (2.17) as a convenient check on the convergence of our numerical method.

2.5. *Numerical implementation*

Both steps of the solution procedure were implemented numerically using Matlab. The first step computes the characteristic map by tracing a finite number of initially

uniformly spaced characteristics from the left interval D_0 to the right interval D_1 by computing each of the maps $R_n(x)$ in succession. This procedure includes an accurate nonlinear computation of the reflection in (2.10) for finite-amplitude topography. We found it convenient to define a function $g(x)=h(x)+x$ and compute its inverse $g^{-1}(x)$ (which exists since the topography is subcritical), so that the characteristic map starting at $x_i \in D_0$ is given inductively by $R_{n+1}(x_i)=R_n(x_i)+2\pi+2(g^{-1}(R_n(x_i)+\pi)-(R_n(x_i)+\pi))$.

The second step solves a truncated version of (2.15) to obtain the spectral coefficients. To obtain good convergence for the energy fluxes, we typically used around 512 characteristics in the first step and around 1024 modes in the second step. Once we know $f(x)$ for $x \in D_0$, we then use (2.12) to obtain $f(x)$ at any desired location, and from this we can compute the streamfunction at any point (x, z) in the domain via (2.7).

3. Wave focusing

In all numerical experiments, we use a single mode-one wave with unit amplitude as the incoming wave field from the left. Of primary interest is the attenuation of the energy flux associated with this mode-one wave as the topography is crossed, which can be interpreted as a degradation of this primary wave and is associated with an energy flux cascade to higher modes. Importantly, the spatial structure of the higher modes that are so generated is tightly focused in space, which leads to significant velocity shears and increased local amplitudes of the wave field. In nature, this would be the first step towards wave breaking and irreversible fluid mixing in the ocean interior.

3.1. *Resonant and non-resonant sinusoidal topography*

In the idealized case of

$$h(x) = \sigma \sin(k_h x) \quad \text{with } \sigma \ll 1 \tag{3.1}$$

in the domain, one can understand the cascade to higher wavenumbers via wave–wave interactions in which the topography plays the role of a zero-frequency wave. Thus, an incoming wave with wavenumber k encountering topography with wavenumber k_h gives rise to new waves with the same frequency but different wavenumbers $k \pm k_h$. These new waves again interact with the topography and the cascade is underway. This wave–wave cascade suggests that it is crucially important whether the topography is *resonant*, i.e. whether k_h is an integer such that the wave–wave interactions can project onto propagating modes of the flat topography system. Indeed, in the resonant case the periodic system resembles a closed container with irregular bottom shape, with the well-known attendant focusing of the waves into narrow zones of attraction (e.g. Maas & Lam 1995). This is because following any characteristic the resonant topography repeats itself over and over, just as it does in a closed container.

This focusing effect is illustrated for the cases $k_h=1$ and $k_h=2$ in figures 3 and 4, respectively. Both plots in each figure show the real and (minus) the imaginary parts of Ψ, which correspond to increasing time by a quarter period. In both cases $\sigma=0.1$. The $k_h=1$ case is special because for small-amplitude topography, it does not lead to back-reflected waves, which are characterized by negative wavenumbers arising from the wave–wave interactions (Chen 2009). This is because the interaction coefficient to generate $k=0$ modes turns out to be zero and hence if $k=1$ and $k_h=1$ then no $k<0$ waves can ever be generated. This is not the case if $k_h=2$, where significant

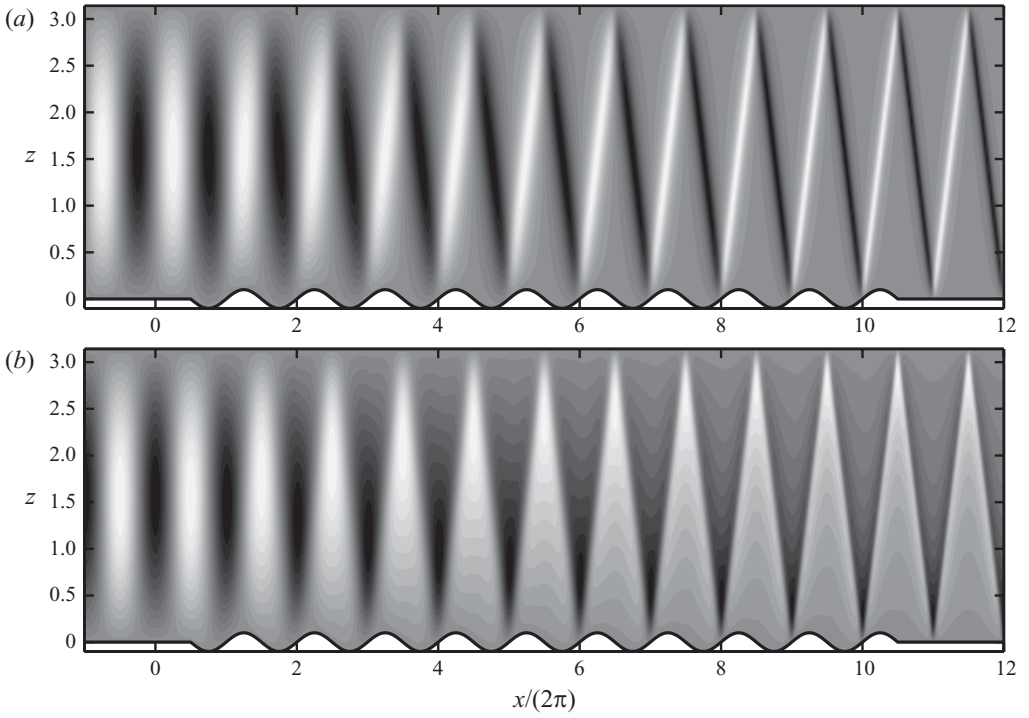

FIGURE 3. Snapshots at $t=0$ (a) and $t=\pi/2$ (b) of $\mathrm{Re}\Psi(x,z)\,\mathrm{e}^{-\mathrm{i}t}$ for resonant topography $h(x)=0.1\sin x$. The fixed-point focusing is evident. There is no back-reflection, and the mode-one transmitted energy flux after 10 bounces is only 17 % of the incoming flux.

back-reflection occurs immediately, which is visible in the difference between the two phase-shifted snapshots in figure 4.

Following previous authors such as Maas & Lam (1995), we can understand the focusing in the resonant case via the characteristic map, as this provides qualitative insight into the geometric structure of the streamfunction. Let $h(x)$ be periodic, with period 2π. We will show that all characteristics are eventually mapped to the same set of points, namely those points modulo 2π such that $\bar{h}(x)=0$, $\bar{h}'(x)>0$, where $\bar{h}(x)=h(x+\pi)$. Indeed, let $r_n(x)=R_n(x)-2\pi n$ describe the fluctuation of the characteristic map about its value for flat topography. Since $\Delta(x)$ is also 2π periodic, the fluctuation evolves according to the autonomous dynamical system

$$r_{n+1}(x) = F(r_n(x)), \quad F(x) := x + 2\Delta(x). \tag{3.2}$$

This has fixed points wherever $\Delta(x)=0$, i.e. wherever $\bar{h}(x)=0$. Assume that there is at least one fixed point $\bar{x}$. Differentiating (2.10) at this point yields $\Delta'(\bar{x})=-\bar{h}'(\bar{x})/(1+\bar{h}'(\bar{x}))$. Therefore, $|F'(\bar{x})|<1 \Leftrightarrow \bar{h}'(\bar{x})>0$, so the fixed point is locally stable exactly when the derivative of the topography at the place where the characteristic reflects off the bottom is positive. This is clearly visible in the figures.

The wave-focusing process is frustrated and essentially absent if the topography is non-resonant. For example, figure 5(a) shows the case $k_h=1.5$, where there is essentially no reflection and no attenuation. This can again be understood by considering the path of a single characteristic, which now hits the topography twice in different phase locations before it repeats the cycle. At each hit, the slope of the

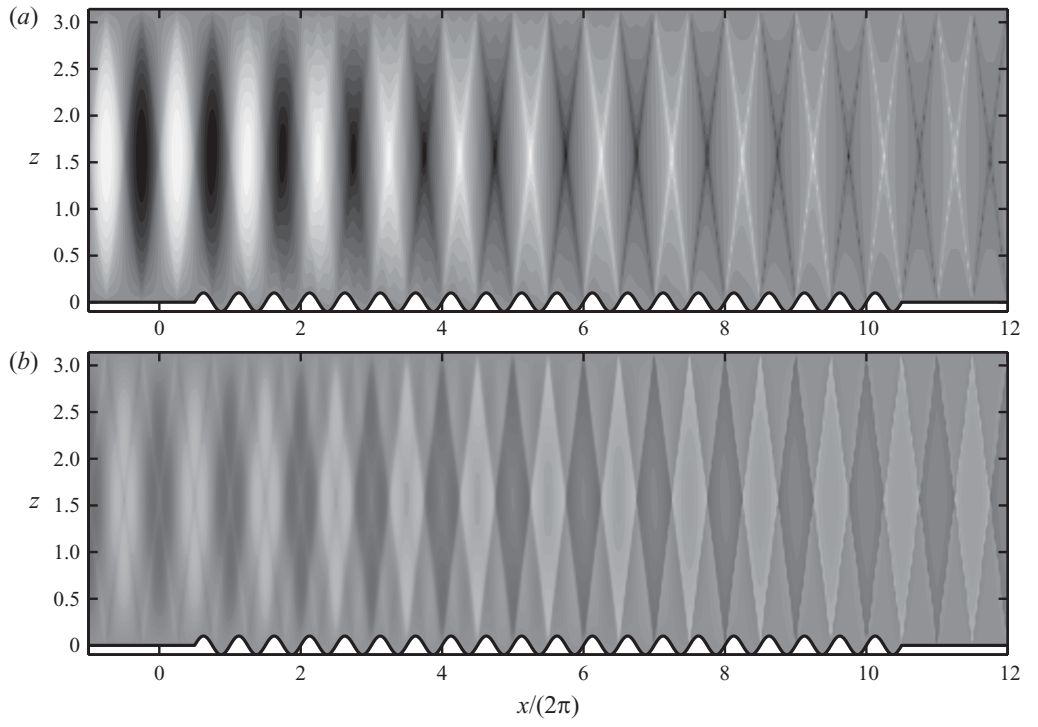

FIGURE 4. Snapshots at $t=0$ (a) and $t=\pi/2$ (b) of $\mathrm{Re}\Psi(x,z)\,\mathrm{e}^{-\mathrm{i}t}$ for resonant topography $h(x)=0.1\sin 2x$. There is significant back-reflection (about 30 %) of wave energy and the transmitted mode-one energy flux is 7 % of the incoming flux.

topography changes sign and this frustrates the focusing. This is robust behaviour, as can be seen in figure 5(b), where the sinusoidal topography has been replaced by a wedge shape with the same period. Indeed, in this case (which could be relevant for laboratory experiments) the characteristic map can be integrated by hand and is precisely periodic, so no cascade can take place even for infinite topography extent.

Therefore, we can conclude that the occurrence of strong wave–topography interactions and wave focusing is confined to resonant topography, i.e. to integer wavenumbers k_h. As an aside, we have experimented with near-resonant sinusoidal topography such that $k_h=1+\epsilon$ with small ϵ, for example. In such a case, we obtain the same mode-one energy flux decay results as for resonant topography, but only if the topography extent is short in the sense that the running length $L\ll 1/\epsilon$. For longer topography the energy flux decay disappears; more precisely, as a function of $L\geqslant 1/\epsilon$ the energy flux then oscillates weakly just below its original value.

3.2. *Energy flux decay*

As a quantitative proxy for the wave focusing, we studied the decay of the energy flux in mode one, the logarithm of which is plotted as a function of topography length in a number of cases in figure 6. Here the topography support is much longer than in the previous examples, with up to 100 bounces. Correspondingly, the decay of the waves is much stronger, about three orders of magnitude, even though the topography amplitudes are quite weak. Figure 6(a) also served as a useful test of our numerical model because in this special, reflectionless case an analytical solution is available for

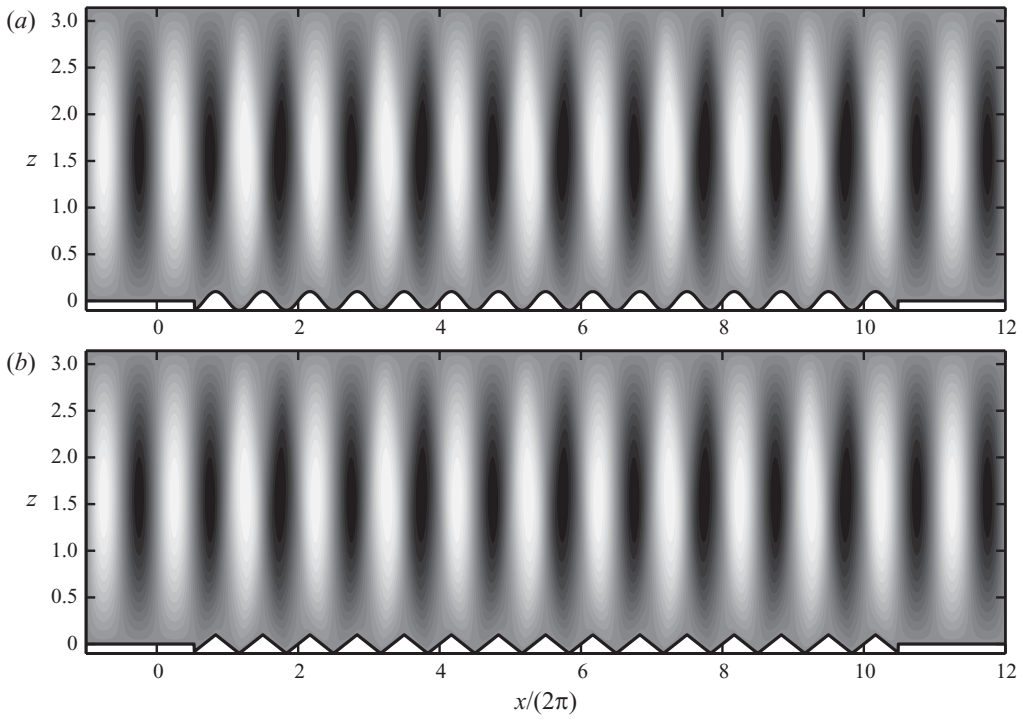

FIGURE 5. (*a*) Snapshot at $t=0$ of $\mathrm{Re}\Psi(x,z)\,\mathrm{e}^{-it}$ for *non-resonant* topography $h(x)=0.1\sin 1.5x$. There is no discernible reflection or attenuation of the mode-one energy flux. (*b*) Same quantity for a wedge-shaped topography for the same period.

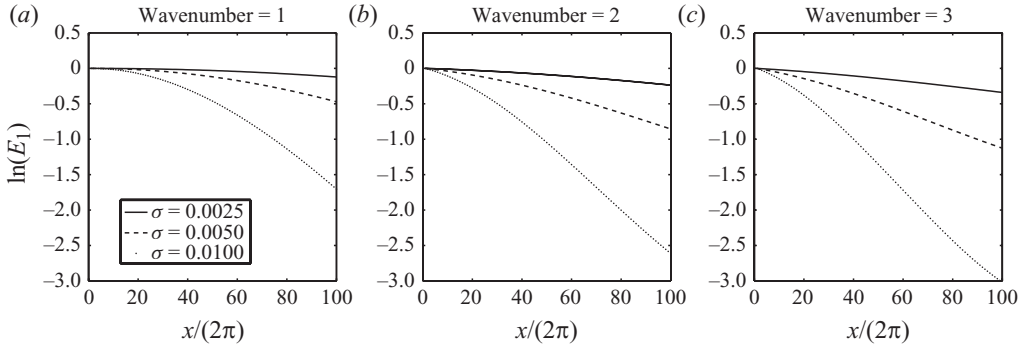

FIGURE 6. Logarithm of energy flux E_1 plotted as a function of topography length in nine cases based on (3.1). (*a–c*) The topography wavenumber $k_h=\{1,2,3\}$ in the three plots, each with the topography amplitude $\sigma=\{0.0025, 0.005, 0.01\}$. The curves for $k_h=1$ in (*a*) agree to plotting accuracy with an analytical solution that is available in this special case (see Appendix).

comparison (see the Appendix); the corresponding curves are indistinguishable from our numerical curves in this plot.

After a transient phase over the first 20 bounces or so, there is evidence of exponential decay with bounce number, i.e. $E_1 \propto \exp(-\lambda n)$ in terms of the bounce number $n=x/(2\pi)$ and a decay rate λ, say. From the numerics, it appears that $\lambda \propto \sigma$ in all cases, which is consistent with the idea of wave–wave interactions between

an exponentially decaying mode-one wave and fixed topography with amplitude σ. There seems to be only a weak dependence of λ on the topography wavenumber k_h, but we could not extract a clear scaling from our results.

It is important to note that the results from this section cannot be used to estimate decay rates due to a superposition of sinusoidal topographies of the form (3.1). This can be understood by considering the characteristic map and the attendant focusing dynamics, which depend sensitively on the local details of the topography and not just on some average amplitude given by its Fourier coefficients. This makes it obvious that we need to consider more complicated model topographies if we want to derive a meaningful result for the real ocean, whose topography is certainly not characterized by a single wavenumber. We address this in the next section, which is devoted to random topography. There, we will find that in a certain limit of *uncorrelated* topography, one can again derive simple scaling relations for the decay rate based on contributions from resonant wavenumbers to the random topography.

4. Random topography

4.1. *Definition of random* $h(x)$

We restrict ourselves to the simplest case of random topography by assuming that $h(x)$ for $x \in [0, L]$ is a section of a zero-mean stationary Gaussian process defined on the real line by its stationary covariance function $C(x)$ such that

$$\mathbb{E}h(x) = 0 \quad \text{and} \quad \mathbb{E}h(x')h(x'+x) = C(x), \tag{4.1}$$

where $\mathbb{E}$ denotes probabilistic expectation. The corresponding Fourier transform is

$$\hat{C}(k) = \int_{-\infty}^{\infty} C(x)\exp(-\mathrm{i}kx)\,\mathrm{d}x \quad \text{and} \quad C(x) = \frac{1}{2\pi}\int_{-\infty}^{\infty} \hat{C}(k)\exp(+\mathrm{i}kx)\,\mathrm{d}k. \tag{4.2}$$

Admissible covariance functions $C(x)$ have real even positive Fourier transforms, e.g.

$$C(x) = \sigma^2 \exp\left(-\frac{x^2}{2\alpha^2}\right) \quad \Leftrightarrow \quad \hat{C}(k) = \sqrt{2\pi}\sigma^2\alpha \exp\left(-\frac{k^2\alpha^2}{2}\right). \tag{4.3}$$

Here $\alpha > 0$ is a length scale such that $\mathbb{E}h^2 = \sigma^2$ and $\mathbb{E}(h'^2) = -C''(0) = \sigma^2/\alpha^2$. We use (4.3) and other simple choices and combine this with standard methods to generate a stationary Gaussian random process on a long interval by using a Fourier series whose coefficients are independent zero-mean Gaussian random variables (see Yaglom 1962; for an application in a fluid's setting see Bühler & Holmes-Cerfon 2009).

Notably, with a choice like (4.3), our topography is random but not rough, i.e. the random function $h(x)$ almost surely has infinitely many continuous derivatives. Indeed, the derivatives of h are themselves zero-mean stationary Gaussian random functions. Regarding the assumption of subcritical topography, we exploit that by making $\mathbb{E}(h'^2) = -C(0)$ small enough we can make the occurrence of supercritical topography in $x \in [0, L]$ for fixed L, an exponentially rare event. In addition, we monitored the maximum of $|h'(x)|$ and discarded topography samples that contained supercritical regions. Expected values were then computed by averaging over 100 independent topography samples.

An important role is played by the correlation scale of the topography. Loosely, we say the topography is *uncorrelated* if $|C(x)| \ll C(0)$ for $x \geqslant 2\pi$, so that the topography that a characteristic encounters on each bounce is uncorrelated with the topography it encountered on previous bounces. We say the topography is *correlated*

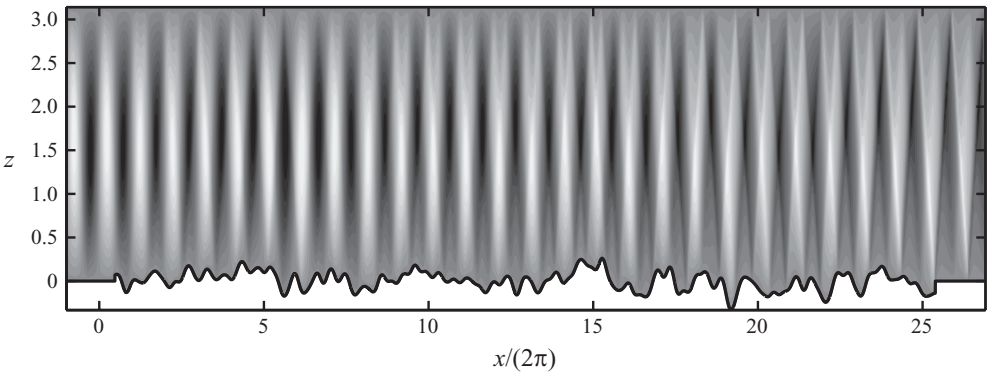

FIGURE 7. Snapshot at $t = 0$ of $\mathrm{Re}\Psi(x, z)\mathrm{e}^{-\mathrm{i}t}$ for uncorrelated random topography using (4.3) with $\sigma = 0.1$ and $\alpha = 1$ over 25 bounces. The wave focusing is clearly visible.

if this condition does not hold. Broadly speaking, in (4.3) the uncorrelated regime corresponds to $\alpha < 2\pi$.

4.2. *Random wave focusing*

Figure 7 shows a run over 25 bounces of uncorrelated small-amplitude random topography based on (4.3) with $\sigma = 0.1$ and $\alpha = 1$. This makes apparent that wave focusing indeed persists for random topography, although the mechanism is somewhat different from that in the previous case of resonant sinusoidal topography, where the topography was of course completely correlated from bounce to bounce. There, following the motion of a single characteristic led to an autonomous dynamical system of the type (3.2) and to the convergence towards the stable fixed points of that system.

On the other hand, in the present random case the topography encountered by following a single characteristic from bounce to bounce is uncorrelated, i.e. the sequence of random topography values that the characteristic encounters at the sea floor is essentially a sequence of identically distributed independent random numbers with zero mean. The same is true for the sequence of values of the shift function, which for small-amplitude topography is $\Delta \approx -h$, and this makes it clear that the characteristic undergoes a discrete random walk in the horizontal with drift 2π and variance of the random step size approximately equal to $\mathbb{E}h^2$.

However, the same is not true for the motion of a pair of two nearby characteristics, separated by a distance small compared to the correlation length α, say. Clearly, the pair will encounter highly correlated values of h and will therefore move in a random walk together. Moreover, should the two characteristics be brought closer together by a random fluctuation, then their correlation will be increased in future bounces, and this provides an irreversible, ratchet-like mechanism for the clustering of nearby characteristics. This mechanism can be observed in figure 8, which illustrates the emergence of steps in the characteristic map with increasing bounce number. These steps are locations where many characteristics are clustered together. The point is that whilst the location of these steps is random, their appearance is completely generic and inevitable.

We can take several steps towards a simple mathematical model for this irreversible process, at least for uncorrelated topography. First, using (2.13) for the evolution of

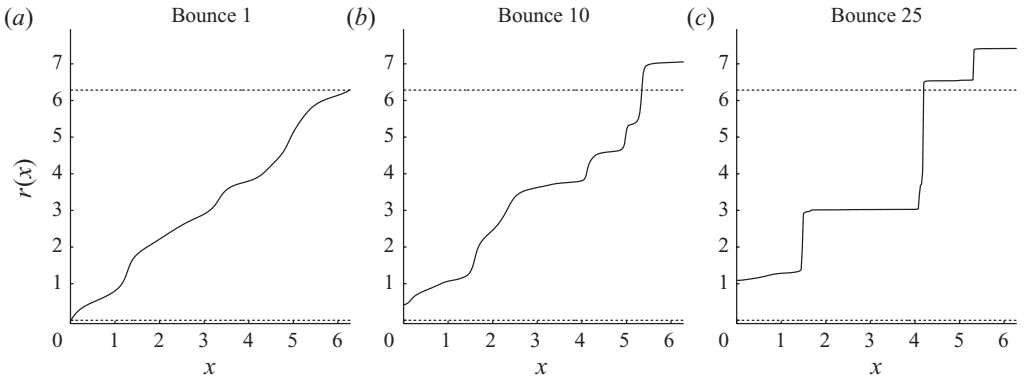

FIGURE 8. (*a–c*) The characteristic map $R_n(x)$ after $n = \{1, 10, 25\}$ bounces for an example based on (4.3) with $\sigma = 0.1$ and $\alpha = 0.4$. After a small number of bounces, the map is a small perturbation of the identity, but after many bounces the map becomes step-like, which indicates that the characteristics are clustered in discrete locations. As the number of bounces increases, the clustering becomes very pronounced, so that there are only a few points that contain almost all of the characteristics. These points move around as random walks, and when they collide they become a single point, until eventually there is only one clustering point left: all the characteristics are mapped onto virtually the same location.

the separation δ_n of neighbouring characteristics leads to

$$\ln \delta_n = \ln \delta_0 + \sum_{m=1}^{n} Z_m, \quad \text{where } Z_m \stackrel{d}{=} \ln\left(\frac{1-s}{1+s}\right) \tag{4.4}$$

and s is the topography slope h' at a bounce location, which for uncorrelated topography has the same distribution at every bounce as indicated by the equality in distribution. Clearly, Z_m are independent identically distributed random numbers and therefore (4.4) describes a random walk of $\ln \delta_n$ in the bounce number n.

Now, if the slope at a bounce location were distributed like the slope at an arbitrary point, then at this stage the distribution of s would be that of a zero-mean Gaussian variable and hence the expected value of the odd function $Z_m(s)$ would then be zero, i.e. $\mathbb{E}Z_m = 0$. In this case, $\ln \delta_n$ would perform a random walk with zero drift, which means that as a function of n the separation δ_n would forever alternate between values above or below its original value. So there would be no irreversible focusing.

However, it turns out that h' at a bounce location is *not* equal in distribution to h' at an arbitrary point. For small-amplitude topography, this can be seen from the shift function Δ in (2.10), which implies that to first order in topography $\Delta = -h(x + \pi)$, where $x + \pi$ is the x-location where the rightward characteristic would hit the sea floor if the topography were flat (cf. figure 2). The slope at the bounce location is therefore

$$s = h'(x + \pi + \Delta) = h'(x + \pi) + \Delta\, h''(x + \pi) = h'(x + \pi) - h(x + \pi)h''(x + \pi) \tag{4.5}$$

correct to second order. The last term has non-zero expectation; in fact, we have

$$\mathbb{E}s = \mathbb{E}h'(x + \pi) - \mathbb{E}h(x + \pi)h''(x + \pi) = 0 + \mathbb{E}h'^2 \geqslant 0 \tag{4.6}$$

for any stationary h'. This shows that $\mathbb{E}s > 0$ at rightward bounce locations and therefore presumably $\mathbb{E}Z_w < 0$ in (4.4). The implication is a negative drift in the random walk of $\ln \delta_n$ and therefore $\ln \delta_n \to -\infty$ almost surely as $n \to \infty$. So, $\delta_n \to 0$ as $n \to \infty$ for almost all starting points, which is consistent with our numerical results.

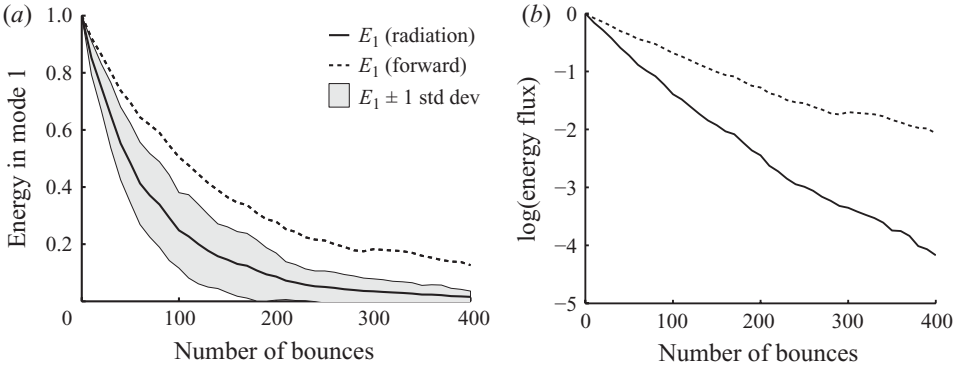

FIGURE 9. (*a*) $E_1(n)$ based on full radiation condition (solid), $\tilde{E}_1(n)$ based on naive specification of incoming wave field (dashed); see text. Shaded area is ± 1 standard deviation away from $E_1(n)$ for each n. (*a,b*) Both plots use (4.3) with $\sigma = 0.05, \alpha = 0.5$ and average over $N_s = 100$ topography samples.

Interestingly, repeating this argument for leftward characteristics would lead to $\mathbb{E}s < 0$ at leftward bounce locations, and again to the irreversible clustering of neighbouring characteristics after many leftward bounces. This must be so because of the left–right symmetry of the characteristic map.

5. Scaling laws for expected energy flux decay

A typical example of our numerical results for the expected value of the mode-one energy flux is plotted in figure 9. In fact, this figure shows two computations, one using the correct radiation condition and the other using the naive approach of simply specifying the wave field on the left to consist of the incoming mode-one wave only. The obvious error illustrates the essential importance of the correct radiation condition.

The logarithmic plot shows clear evidence of exponential decay of the expected energy flux; that this should be so at least initially appears plausible: when the energy flux in the primary wave is large compared to the energy flux in the other modes, the main flow of energy is from the mode-one wave to the higher modes, so the amount transferred in each bounce is proportional to the energy flux in the primary wave. Still, the variance around the exponential decay is quite large, as also indicated in the figure, and individual topography samples can produce quite different decay profiles for the energy flux. However, the exponential decay appears robust for the expected value of the energy flux.

On the basis of this result, we define a statistical decay rate λ_1 via

$$\lambda_1 : \quad E_1(n) = \mathbb{E}|a_1^t|^2 = \mathrm{e}^{-\lambda_1 n}. \tag{5.1}$$

We want to investigate how λ_1 depends on the details of the covariance function and for uncorrelated topography we expect the two important parameters to be the variance of h and its slope h'. For the specific covariance in (4.3), we can adjust the explicit parameters σ and α, and for any other choice of covariance function we can achieve the same by scaling the random topography via

$$h(x) \to \sigma h(x/\alpha), \quad C(x) \to \sigma^2 C(x/\alpha) \tag{5.2}$$

and therefore $\mathbb{E}h^2 \to \sigma^2 \mathbb{E}h^2$ and $\mathbb{E}h'^2 \to \sigma^2 \alpha^{-2} \mathbb{E}h'^2$.

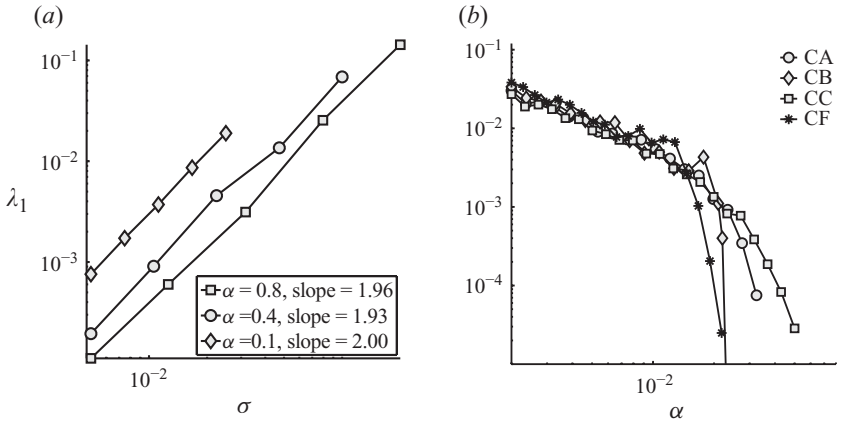

FIGURE 10. (*a*) Mode-one decay rate λ_1 as a function of σ, for (4.3) with three different values of α. The slopes of the best-fit lines for all are very close to 2. (*b*) Mode-one decay rate λ_1 for a variety of covariance functions as a function of α, showing $\lambda_1 \propto \alpha^{-1}$ for small α and a sharp drop off for $\alpha \geqslant 1$, which corresponds to correlated topography. Details of the covariance functions are given in the Appendix and all plots are ensemble averages with $N_s = 20$ and $\sigma = 0.05$.

5.1. *Scaling of decay rate λ_1 with σ and α*

Figure 10(*a*) shows results for λ_1 obtained by varying σ at fixed α. The logarithmic plots show a clear slope of two, i.e. we have the quadratic scaling $\lambda_1 \propto \sigma^2$ for uncorrelated random topography. This is clearly different from the linear scaling $\lambda \propto \sigma$ that we observed in the case of deterministic sinusoidal topography. The reason is that at first order in σ the topography encountered along the characteristic map in the random case simply fluctuates around zero. It is only at second order in σ that the random walk of the foot point is felt.

Figure 10(*b*) also shows that there is a simple scaling with α for fixed σ, but only in the regime of uncorrelated topography, i.e. for α not too large. In this regime, we found that $\lambda_1 \propto \alpha^{-1}$, but we have no simple convincing theoretical argument in its favour. Again, this scaling is very different from that of the case of sinusoidal topography, where the decay rate was broadly independent of the wavenumber k_h. (As an aside, this scaling only holds when the radiation condition is implemented correctly, otherwise the rates are significantly different.) Combining the two scalings we can conclude that $\lambda_1 \propto \sigma^2 \alpha^{-1}$ in the regime of uncorrelated random topography. This can be written in terms of the standard deviations of the topography and its derivative as

$$\lambda_1 = \Gamma_0 \sigma_h \beta_h, \quad \text{where } \sigma_h^2 = \mathbb{E}|h|^2, \quad \beta_h^2 = \mathbb{E}|h'|^2, \tag{5.3}$$

and Γ_0 is the proportionality constant. The value of Γ_0 depends on the shape of the covariance function, but we found that it varies very little for reasonable functions; this can be seen in figure 10. The discussion in § 5.3 suggests that $\Gamma_0 \leqslant \pi$ in general and that $\Gamma_0 = 2.5$ for a Gaussian covariance function.

For larger α the assumption of uncorrelated topography eventually breaks down, and in this regime the rate drops off sharply, as can be seen in figure 10(*b*). Also, the precise shape of the covariance function then begins to matter. We found no simple scaling that applies to correlated random topography, but see § 5.3 for a more general formula based on the Fourier transform of the covariance function.

5.2. *A surprising dimensional decay rate*

The non-dimensional scaling (5.3) for uncorrelated topography has a surprising physical implication when translated back into dimensional units. Using the ocean depth H as before, writing the dimensional topography as $\tilde{h} = (H/\pi)h$, and noting that the dimensional length of a bounce is $2H/\mu$ then gives a dimensional rate of decay per unit length of topography of

$$\tilde{\lambda}_1 = \frac{\pi \Gamma_0}{2H^2} \sqrt{\mathbb{E}|\tilde{h}|^2 \mathbb{E}|\tilde{h}'|^2}. \tag{5.4}$$

This means that the expected energy flux should decay as $\exp(-\tilde{\lambda}_1 \tilde{x})$ along the dimensional running length $\tilde{x} = xH/(\pi\mu)$. The upshot of (5.4) is that if we know that the topography is uncorrelated, then we can estimate the rate of mode-one energy decay entirely from the point-wise statistics $\mathbb{E}|\tilde{h}|^2$, $\mathbb{E}|\tilde{h}'|^2$ and without knowing anything else about the problem.

Now, this formula is very surprising because it contains *neither* of the three frequencies N, f and ω that arise in the physical problem definition. Therefore, the wave slope μ is also absent here. Thus, it appears that changing N or f or ω does not affect the dimensional decay rate $\tilde{\lambda}_1$.

This result could not have been guessed from dimensional analysis, because there is no *a priori* argument to rule out a dependence of $\tilde{\lambda}_1$ on the non-dimensional parameters ω/f and f/N, say. Of course, this result does depend on the implicit assumptions that have been made, namely that $f \leqslant \omega \leqslant N$, that the topography is subcritical, and that the topography is uncorrelated, but otherwise its scope is considerable.

5.3. *Towards an explicit formula for the damping rate*

We have made several attempts to derive an analytic expression for the damping rate λ_1 in the case of infinitesimal topography. These attempts met with some success in that we identified what seems to be the correct formula for λ_1, but we cannot derive it convincingly. Nevertheless, we hope our partial results are instructive and hence present them briefly here.

One such attempt was based on an expansion of the streamfunction in vertical modes with x-dependent amplitude coefficients $a_n(x)$, say. The interaction with infinitesimal random topography then leads to a system of differential evolution equations in x for the modal amplitudes $a_n(x)$. This random ODE system can then be analysed for large x using a diffusion approximation for the amplitudes based on the general theory for random ODEs laid out in Papanicolaou & Kohler (1974). This led us to results similar in form to those of Nachbin & Papanicolaou (1992). A second attempt was based on working in real space with the characteristic map by trying to solve the joint evolution of many characteristics together with an approximate treatment of the radiation condition.

We were not able to derive rigorously an asymptotic formula for λ_1 using either approach, but we can report on a partial result, namely that both approaches suggested an expression for λ_1 of the form

$$\lambda_1 = \sum_{k=1}^{+\infty} k \hat{C}(k), \tag{5.5}$$

where $\hat{C}(k)$ is the Fourier transform of the covariance function as before. This expression performed fairly well in our numerical tests, especially for correlated

topography. Actually, both our theoretical attempts led to formulae that were close to (5.5), but differed by pre-factors of order unity that made the quantitative agreement with our numerical results worse. Also, we are aware that this sum over resonant wavenumbers is tantalizingly close to the formulae for the energy conversion from a barotropic tide over localized deterministic topography that are summarized by Khatiwala (2003), but we did not find it straightforward to adapt the methods used there to the case at hand.

Now, for uncorrelated topography and $\alpha \to 0$, the expression (5.5) is indeed consistent with the scalings we found previously. This follows because $\hat{C}(k) \to \sigma^2 \alpha \hat{C}(k\alpha)$ under the scaling transformation (5.2), and therefore as $\alpha \to 0$ we have

$$\alpha\lambda_1 \to \sigma^2 \sum_{k=1}^{+\infty} (k\alpha)\hat{C}(k\alpha)\,\alpha \approx \sigma^2 \int_0^\infty s\hat{C}(s)\,\mathrm{d}s \propto \sigma^2. \tag{5.6}$$

For the Gaussian covariance function in (4.3), this leads to $\lambda_1 = (\sigma^2/\alpha)\sqrt{2\pi} \approx 2.5(\sigma^2/\alpha)$, which is origin of the value $\Gamma_0 = 2.5$ in (5.3) that we used before.

Notably, the expression (5.5) is not restricted to the uncorrelated case, and therein lies its main utility. For example, experimenting with this formula corroborated the results from figure 10: at fixed $\mathbb{E}h^2$ and $\mathbb{E}h'^2$ the transition to correlated topography leads to a reduction of the damping rate λ_1.

Finally, the equivalent expression to (5.5) in dimensional form is

$$\tilde{\lambda}_1 = \frac{\pi}{2H^2} \sum_{k=1}^{\infty} \frac{\pi\mu k}{H} \hat{\tilde{C}} \left(\frac{\pi\mu k}{H} \right) \frac{\pi\mu}{H}, \tag{5.7}$$

which allows estimating $\tilde{\lambda}_1$ directly from data for the dimensional topography covariance function. Here the laboured notation $\hat{\tilde{C}}$ denotes the Fourier transform of the dimensional covariance function $\tilde{C}(\tilde{x}) = \mathbb{E}\tilde{h}(0)\tilde{h}(\tilde{x})$. Deriving (5.7) from (5.5) uses the relations $C(x) = (\pi^2/H^2)\tilde{C}(\tilde{x})$ and $\hat{C}(k) = (\mu\pi^3/H^3)\hat{\tilde{C}}(\tilde{k})$, which follow from the definition of the Fourier transform together with $x = (\mu\pi/H)\tilde{x}$ and $\tilde{k}\tilde{x} = kx$.

For fixed topography, the limit of uncorrelated topography for this expression corresponds to $\mu \to 0$, and by the same limit used in (5.6) we now obtain

$$\tilde{\lambda}_1 \to \frac{\pi}{2H^2} \int_0^\infty \tilde{k}\hat{\tilde{C}}(\tilde{k})\,\mathrm{d}\tilde{k}. \tag{5.8}$$

This is consistent with (5.4) because for $\hat{\tilde{C}}(\tilde{k}) \geqslant 0$ we have that

$$\int_0^\infty \tilde{k}\hat{\tilde{C}}(\tilde{k})\,\mathrm{d}\tilde{k} \leqslant \sqrt{\int_0^\infty \hat{\tilde{C}}(\tilde{k})\,\mathrm{d}\tilde{k} \int_0^\infty \tilde{k}^2\hat{\tilde{C}}(\tilde{k})\,\mathrm{d}\tilde{k}} = \pi\sqrt{\mathbb{E}\tilde{h}^2\mathbb{E}\tilde{h}'^2} \tag{5.9}$$

by the Cauchy–Schwarz inequality based on $\sqrt{\hat{\tilde{C}}}$ and $\tilde{k}\sqrt{\hat{\tilde{C}}}$. Thus, for uncorrelated topography we showed that $\Gamma_0 \leqslant \pi$ in (5.4), which is obviously satisfied for the value $\Gamma_0 = \sqrt{2\pi}$ that we obtained for a Gaussian covariance function.

In summary, (5.7) is our best, most accurate formula for computing the dimensional decay rate $\tilde{\lambda}_1$ for both correlated and uncorrelated topography, (5.8) is a simpler form valid only for uncorrelated topography, and (5.4) with $\Gamma_0 = 2.5$ is the simplest form valid for uncorrelated topography, which requires only root-mean-square information about the topography and its slope.

6. Application to model spectra for small-scale ocean topography

We can use our model to investigate how topography in the real ocean might scatter and degrade a mode-one internal tide. First, we used the analytic spectrum for topography created by Bell (1975). This is an isotropic power-law spectrum for topography intended to model the abyssal hill region of the ocean basin away from large features such as ridges. Specifically, the spectrum is defined such that the variance of $\tilde{h}(x, y)$ is

$$\mathbb{E}\tilde{h}^2 = (125\,\mathrm{m})^2 \int_0^{\kappa_2} \frac{\kappa_1 \kappa}{\left(\kappa^2 + \kappa_1^2\right)^{3/2}}\,\mathrm{d}\kappa \quad \text{with } (\kappa_1, \kappa_2) = \left(\frac{2\pi}{40\,\mathrm{km}}, \frac{2\pi}{400\,\mathrm{m}}\right). \tag{6.1}$$

Here κ_1 controls the correlation length of the topography and κ_2 is a cutoff scale that regulates the slope variance $\mathbb{E}|\nabla\tilde{h}|^2 = (125\ \mathrm{m})^2\kappa_1\kappa_2 \approx 0.2^2$.

The spectrum is for 2D topography, i.e. $\kappa^2 = k^2 + l^2$, so to apply it to our results for 1D topography we make the modelling assumptions that our results are valid on any 2D plane through the ocean and we calculate the spectrum for the topography in k-space as the marginal spectrum of the topography in the (k, l)-space. The variance of the derivative can then be found using $|\nabla\tilde{h}|^2 = \tilde{h}_x^2 + \tilde{h}_y^2$ and noting that each of these has the same expected value by horizontal isotropy, so a 1D slice of topography has $\mathbb{E}|\tilde{h}'|^2 = (125\,\mathrm{m})^2\kappa_1\kappa_2/2 = (0.14)^2$. Subject to the normalization in (4.2), the resultant spectrum corresponds to $\hat{\tilde{C}}(k)$ in § 5.3.

To compute the dimensional decay scale $\tilde{\lambda}_1$ for the mode-one energy flux from our best formula (5.7), we need to set the ocean depth H and the wave slope μ. Using $H = 4\,\mathrm{km}$ and $\mu = 0.17$ based on $N/f = 10$ and $\omega/f = 2$, we obtain a decay scale $\tilde{\lambda}_1 \approx 500\,\mathrm{km}$. If $H = 5\,\mathrm{km}$ is used instead then we obtain $\tilde{\lambda}_1 \approx 800\,\mathrm{km}$. We verified these values using direct Monte-Carlo simulations for scattering off Bell's topography. These results are not very sensitive to the value of μ, i.e. the results are nearly identical to the expression (5.8) that holds as $\mu \to 0$. However, these results depend strongly on the parameters of Bell's spectrum. In particular, due to the relatively slow decay of the spectrum at high wavenumbers, the sum in (5.7) depends on the wavenumber cutoff. Moreover, the parameters of Bell's topography apparently tend to overestimate the topography amplitudes in much of the Pacific ocean basin.

We therefore repeated our calculations using the more recent model spectrum proposed by Goff & Jordan (1988). The isotropic version of that spectrum is proportional to (6.1) but with the power-law exponent 3/2 replaced by an adjustable constant. We used the same parameter values as in the recent study Nikurashin & Ferrari (2010), where the parameters were fitted to observational data from a southeast Pacific region. This produced an ocean depth of $H = 5\,\mathrm{km}$, a topography standard deviation of 155 m, a correlation length for the topography of 50 km and a power-law exponent of 3.5/2 replacing 3/2 in (6.1). With this faster decay the sum in (5.7) actually converges and with the wave slope $\mu = 0.17$ we then obtained a decay scale of $\tilde{\lambda}_1 \approx 1200\,\mathrm{km}$.

Overall, in comparison with the recent observational case study of long-lived propagating mode-one waves in the Pacific Ocean in Zhao *et al.* (2010), our decay-scale estimates of about 1000 km for the energy flux appear rather short (of course, decay-scale estimates for the *amplitude* of mode-one waves would be a factor of two larger). The obvious candidates for explaining this discrepancy between the observations and our model results are the restriction to linear 2D fluid dynamics and the restriction to uniform stratification in our model. These restrictions are briefly discussed in the next section.

7. Concluding comments

For practical application in oceanography the most useful results reported here are the expressions for the dimensional mode-one energy flux decay rate $\tilde{\lambda}_1$ given in (5.7) together with its simpler, but less general, forms (5.8) and (5.4). Based on how much observational data are available, evaluation of either of these expressions would allow a ready estimate for the prevailing decay rate. This should be especially useful in conjunction with the high-resolution topography data that are increasingly becoming available along research ship tracks, but to look at the present data is beyond the scope of this short paper.

We also think that for laboratory experiments with deterministic topography shapes, the scaling laws in § 3.2 and the numerical tool for computing the detailed wave field should be useful. Again, our numerical tool is based on subcritical but otherwise $O(1)$ topography, so it goes beyond linear theory in topography.

From a modelling point of view, a glaring shortcoming is the restriction to two spatial dimensions. Even if the incoming wave field should be to a good approximation two-dimensional (say because it was generated by tidal conversion at a long ridge), it is certainly not the case that the rough sea floor has 1D topography. The hyperbolic ill-posed nature of the scattering problem persists in three dimensions, although naturally the tight propagation of information along characteristic lines is replaced there by the less tight propagation concentrated around characteristic cones (see e.g. Bühler & Muller 2007 for a comparison between the 2D and 3D versions of the tidal conversion problem). Overall, based on past experience we would expect the three-dimensional details to be significantly more complicated, but that the basic results for the 2D decay rates computed here will be a good approximation to the 3D case. Simple laboratory experiments might be useful in this regard; such experiments could also check whether the strong assumption of constant buoyancy frequency N for the ocean does indeed give a good answer here, as we previously argued based on the recent results in Grimshaw *et al.* (2010).

Another significant shortcoming is the restriction to linear wave dynamics. Nonlinear effects such as wave–wave interactions and higher-order corrections to the boundary conditions could conceivably modify the wave field over long times and therefore over long propagation distances. Such nonlinear effects would naturally lead to additional waves with a different frequency, with unclear consequences for the primary mode-one wave. For example, the surprising independence of the decay rate $\tilde{\lambda}_1$ on the wave slope μ that we found in linear theory might no longer hold under nonlinear dynamics. Presumably, addressing these questions would require nonlinear numerical simulations over long propagation distances.

Finally, from a heuristic point of view, we do not have a ready explanation for the *reduction* of the decay rate when the topography begins to be correlated, even though this reduction is apparent in numerical results depicted in figure 10(*b*). One untested hypothesis for this effect is based on the characteristic map and the covariance function for the slope h', which for $C(x)$ in (4.3) would be

$$\mathbb{E}h'(0)h'(x) = -C''(x) = \frac{\sigma^2}{\alpha^2}\left(1 - \frac{x^2}{\alpha^2}\right)\exp\left(\frac{-x^2}{2\alpha^2}\right). \tag{7.1}$$

This has a range of significant *negative* values (roughly in the interval $1 \leqslant x/\alpha \leqslant 3$, say), and this suggests that for correlated topography a positive value of h' at the present bounce is more likely to be followed by a negative value h' at the next bounce. This anti-correlation would in part cancel the focusing of the nearby characteristics

described by (2.13). So, this could be a candidate mechanism for decreasing the efficiency of random wave focusing for correlated topography.

The research reported here grew out of a summer project undertaken in collaboration with Erinna Chen and Neil Balmforth at the 2009 Woods Hole summer in Geophysical Fluid Dynamics (see Chen 2009), and we acknowledge several stimulating conversations in this regard, including several with N. Grisouard. Further stimulus was provided at the recent Banff Internal Wave meeting in April 2010 and we gladly acknowledge the organizers of that meeting. The comments of several referees significantly improved our manuscript. Financial support for this work under the United States National Science Foundation grant DMS-0604519 is gratefully acknowledged. M.H.-C. was supported in part by a Canadian NSERC PGS-D scholarship.

Appendix

A.1. *Energy flux formula for reflectionless decay*

For infinitesimal sinusoidal topography with wavenumber $k_h = 1$, there are no reflected waves and this allows an analytic solution for the transmitted waves to be found using a multi-scale technique, which leads to the expression (75) in Chen (2009). In the notation used in the present paper, the energy flux in the first mode is then predicted to be

$$E_1(x) = \left(1 - \tanh^2\left(\frac{\sigma x}{2\pi}\right)\right)^2. \tag{A 1}$$

This is indistinguishable from the numerical results plotted in figure 6(*a*).

A.2. *Details of covariance functions used in figure 10*

The covariance functions used in figure 10 are defined by their Fourier transforms as

$$CA: \quad \hat{C}(k) = \sqrt{2\pi}\exp\left(-\tfrac{1}{2}k^2\right), \tag{A 2}$$

$$CB: \quad \hat{C}(k) = \frac{3\pi}{2}(1-k^2) \quad \text{if } |k| \leqslant 1, \text{ zero otherwise}, \tag{A 3}$$

$$CC: \quad \hat{C}(k) = \pi\exp(-|k|), \tag{A 4}$$

$$CF: \quad \hat{C}(k) = \sqrt{\pi}(\exp[-(k-2)^2] + \exp[-(k+2)^2]). \tag{A 5}$$

REFERENCES

Alford, M. H. 2003 Redistribution of energy available for ocean mixing by long-range propagation of internal waves. *Nature* **423**, 159–162.

Arnold, V. I. & Khesin, B. A. 1998 *Topological Method in Hydrodynamics*. Springer.

Balmforth, N. J., Ierley, G. R. & Young, W. R. 2002 Tidal conversion by subcritical topography. *J. Phys. Oceanogr.* **32**, 2900–2914.

Balmforth, N. J. & Peacock, T. 2009 Tidal conversion by supercritical topography. *J. Phys. Oceanogr.* **39** (8), 1965–1974.

Bell, T. H. 1975 Statistical features of sea-floor topography. *Deep-Sea Res.* **22** (12), 883–892.

Bühler, O. 2009 *Waves and Mean Flows*. Cambridge Monographs on Mechanics. Cambridge University Press.

Bühler, O. & Holmes-Cerfon, M. 2009 Particle dispersion by random waves in rotating shallow water. *J. Fluid Mech.* **638**, 5–26.

Bühler, O. & Muller, C. M. 2007 Instability and focusing of internal tides in the deep ocean. *J. Fluid Mech.* **588**, 1–28.

Chen, E. 2009 Degradation of the internal tide over long bumpy topography. In *Proc. Annual Summer Study in Geophysical Fluid Dynamics*, pp. 248–268. Woods Hole Oceanographic Institution.

Echeverri, P. & Peacock, T. 2010 Internal tide generation by arbitrary two-dimensional topography. *J. Fluid Mech.* **659**, 247–266.

Garrett, C. 2003 Internal tides and ocean mixing. *Science* **301**, 1858–1859.

Garrett, C. & Kunze, E. 2007 Internal tide generation in the deep ocean. *Annu. Rev. Fluid Mech.* **39**, 57–87.

Goff, J. & Jordan, T. 1988 Stochastic modelling of seafloor morphology: inversion of sea beam data for second-order statistics. *J. Geophys. Res.* **93** (B11), 13 589–13 608.

Grimshaw, R., Pelinovsky, E. & Talipova, T. 2010 Nonreflecting internal wave beam propagation in the deep ocean. *J. Phys. Oceanogr.* **40** (4), 802–813.

Harlander, U. & Maas, L. R. M. 2007 Two alternatives for solving hyperbolic boundary value problems of geophysical fluid dynamics. *J. Fluid Mech.* **588**, 331–351.

Khatiwala, S. 2003 Generation of internal tides in an ocean of finite depth: analytical and numerical calculations. *Deep-Sea Res.* I. *Oceanogr. Res. Papers* **50** (1), 3–21.

Kunze, E. & Llewellyn Smith, S. G. 2004 The role of small-scale topography in turbulent mixing of the global ocean. *Oceanography* **17**, 55–64.

Llewellyn Smith, S. G. & Young, W. R. 2003 Tidal conversion at a very steep ridge. *J. Fluid Mech.* **495**, 175–191.

Longuet-Higgins, M. S. 1969 On the reflexion of wave characteristics from rough surfaces. *J. Fluid Mech.* **37**, 231–250.

Maas, L. R. & Lam, F. P. 1995 Geometric focusing of internal waves. *J. Fluid Mech.* **300**, 1–41.

Muller, C. M. & Bühler, O. 2009 Saturation of the internal tides and induced mixing in the abyssal ocean. *J. Phys. Oceanogr.* **39**, 2077–2096.

Muller, P. & Liu, X. B. 2000*a* Scattering of internal waves at finite topography in two dimensions. Part I. Theory and case studies. *J. Phys. Oceanogr.* **30** (3), 532–549.

Muller, P. & Liu, X. B. 2000*b* Scattering of internal waves at finite topography in two dimensions. Part II. Spectral calculations and boundary mixing. *J. Phys. Oceanogr.* **30** (3), 550–563.

Muller, P. & Xu, N. 1992 Scattering of oceanic internal gravity-waves off random bottom topography. *J. Phys. Oceanogr.* **22** (5), 474–488.

Nachbin, A. & Papanicolaou, G. C. 1992 Water waves in shallow channels of rapidly varying depth. *J. Fluid Mech.* **241**, 311–332.

Nikurashin, M. & Ferrari, R. 2010 Radiation and dissipation of internal waves generated by geostrophic motions impinging on small-scale topography: application to the southern ocean. *J. Phys. Oceanogr.* **40**, 2025–2042.

Papanicolaou, G. C. & Kohler, W. 1974 Asymptotic theory of mixing stochastic ordinary differential equations. *Commun. Pure Appl. Math.* **27**, 641–668.

Petrelis, F., Smith, S. L. & Young, W. R. 2006 Tidal conversion at a submarine ridge. *J. Phys. Oceanogr.* **36** (6), 1053–1071.

Sobolev, S. L. 1954 On a new problem in mathematical physics. *Izvestia Akad. Nauk SSSR* **18**, 3–50.

St Laurent, L. & Garrett, C. 2002 The role of internal tides in mixing the deep ocean. *J. Phys. Oceanogr.* **32** (10), 2882–2899.

Wunsch, C. & Ferrari, R. 2004 Vertical mixing, energy, and the general circulation of the oceans. *Annu. Rev. Fluid Mech.* **36**, 281–314.

Yaglom, A. M. 1962 *An Introduction to the Theory of Stationary Random Functions*. Dover.

Zhao, Z., Alford, M. H., MacKinnon, J. A. & Pinkel, R. 2010 Long-range propagation of the semidiurnal tide from the Hawaiian ridge. *J. Phys. Oceanogr.* **40**, 713–736.